International Journal of Biological Macromolecules 235 (2023) 123874

Contents lists available at ScienceDirect

International Journal of Biological Macromolecules

journal homepage: www.elsevier.com/locate/ijbiomac

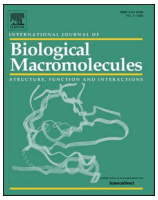

Facile synthesis of copolymerized cellulose grafted hydrogel doped calcium oxide nanocomposites with improved antioxidant activity for anti-arthritic and controlled release of doxorubicin for anti-cancer evaluation

Iram Shahzadi [a], Muhammad Islam [a,*], Hamid Saeed [a], Anum Shahzadi [b], Junaid Haider [c], Ali Haider [d], Muhammad Imran [e], Hassaan Anwer Rathore [f], Anwar Ul-Hamid [g,*], Walid Nabgan [h,*], Muhammad Ikram [i,*]

[a] Punjab University College of Pharmacy, Allama Iqbal Campus, University of the Punjab, Lahore 54000, Punjab, Pakistan
[b] Faculty of Pharmacy, The University of Lahore, Lahore 54000, Pakistan
[c] Tianjin Institute of Industrial Biotechnology, Chinese Academy of Sciences, Tianjin 300308, PR China
[d] Department of Clinical Sciences, Faculty of Veterinary and Animal Sciences, Muhammad Nawaz Shareef University of Agriculture, Multan 66000, Punjab, Pakistan
[e] Department of Chemistry, Government College University, Faisalabad, Sahiwal Road, Sahiwal, Punjab 57000, Pakistan
[f] College of Pharmacy, Q U Health, Qatar University, Doha 2713, Qatar
[g] Core Research Facilities, King Fahd University of Petroleum & Minerals, Dhahran 31261, Saudi Arabia
[h] Departament d'Enginyeria Química, Universitat Rovira i Virgili, Av Països Catalans 26, 43007 Tarragona, Spain
[i] Solar Cell Applications Research Lab, Department of Physics, Government College University Lahore, Lahore 54000, Punjab, Pakistan

ARTICLE INFO

Keywords:
Cellulose nanocrystals
Poly-acrylic acid
Nanocomposites hydrogel

ABSTRACT

The combination treatment is considered an approach to attaining synergistic impact while minimizing applied dosage. Hydrogels are analogous to the tissue environment attributed to hydrophilic and porous structure. Despite extensive study in biological and biotechnological domains, their restricted mechanical strength and limited functionalities impede their potential uses. Emerging strategies are centred on research and developing nanocomposite hydrogels to combat these issues. Herein, we prepared copolymerized hydrogel by grafting poly-acrylic acid P(AA) onto cellulose nanocrystals (CNC) and adding CNC-g-PAA as dopant (2 and 4 wt%) in calcium oxide (CaO) nanoparticles to generate an effective hydrogel doped nanocomposite (NCH) (CNC-g-PAA/CaO) for biomedical applications such as anti-arthritic, anti-cancer, and antibacterial investigations alongside their comprehensive characterization. CNC-g-PAA/CaO (4 %), compared to other samples, had a substantially higher antioxidant potential (72.21 %). Doxorubicin, a potential chemotherapeutic drug, was then effectively loaded into NCH (99 %) via electrostatic interaction, and pH-triggered based release was found to be >57.9 % in 24 h. Furthermore, molecular docking investigation against targeted protein Cyclin-dependent kinase 2 and in vitro cytotoxicity study verified the improved antitumor effectiveness of CNC-g-PAA and CNC-g-PAA/CaO. These outcomes indicated that hydrogels might serve as potential delivery vehicles for innovative multifunctional biomedical applications.

1. Introduction

Integrating nanotechnology with other scientific disciplines, such as the fabrication of multifunctional polymer-based matrices for controlled drug administration, has been the focus of intensive study in the preceding decades [1]. After multiple attempts to combine nano-scale procedures with traditional techniques for producing quality materials, research shifted toward developing polymers and hydrogels as intelligent/smart materials [2,3]. Hydrogels or aqua gels are comprised of natural or synthetic polymer chains, chemically or physically cross-linked, to form a hydrophilic substance with a mucilaginous macromolecular structure [4,5]. Also, a water-insoluble, 3-D polymer matrix may imbibe up to hundreds of times its dry weight in water or biological fluid without compromising structural integrity. This network

* Corresponding authors.
E-mail addresses: anwar@kfupm.edu.sa (A. Ul-Hamid), walid.nabgan@urv.cat (W. Nabgan), dr.muhammadikram@gcu.edu.pk, islam.pharmacy@pu.edu.pk (M. Ikram).

https://doi.org/10.1016/j.ijbiomac.2023.123874
Received 22 December 2022; Received in revised form 13 February 2023; Accepted 25 February 2023
Available online 2 March 2023

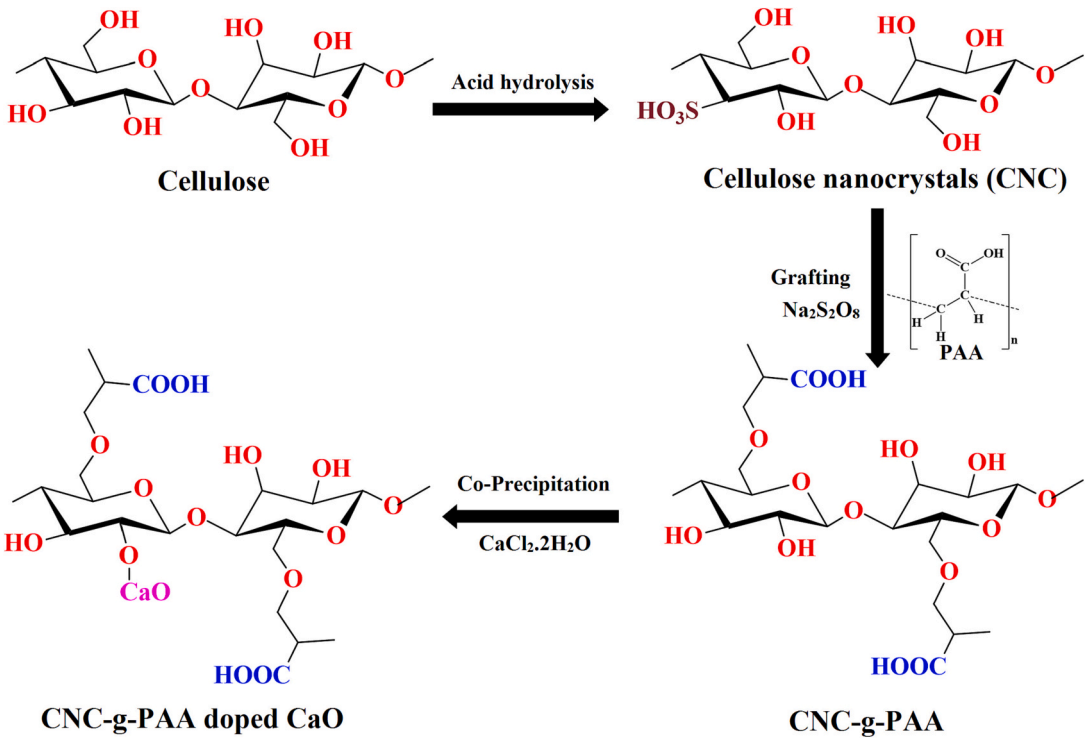

Fig. 1. (a) Chemical structure of cellulose nanocrystals from Cellulose (Avicel) by acid hydrolysis and further grafting of poly-acrylic acid onto CNC, and then CNC-g-PAA was doped at CaO for the formation of CNC-g-PAA/CaO

is hydrophilic owing to functional units, including hydroxyl (—OH), carboxyl (—COOH), amine (NH_2), and sulphate groups (SO_3H^-) [6,7]. Considering the source, natural polymers are advantageous due to enhanced biodegradability and biocompatibility [8,9] but lack dependability and consistency because of their natural origin, culminating in substantial batch-to-batch fluctuations.

Conversely, synthetic polymeric composites are highly repeatable with precisely controlled chemical and physical characteristics. Nevertheless, these are often less compatible than natural polymers, mainly because of material characteristics or detrimental residues originating from production process, that frequently contain cytotoxic or non-biocompatible chemical solvents, initial monomers, or by-products. By merging synthetic and natural polymers, one may reap the benefits of both materials while minimizing or ideally eliminating their specific drawbacks [10], like many commercially available dressing products are composed of synthetic and natural polymers [9].

Despite their significant advantages, aqua-gels have numerous drawbacks, such as low mechanical strength, poor heat stability, and limitations in biomedical applications like poor anti-tumour capacity, weak bioimaging capability, inadequate responsiveness, etc., which restricts the hydrogels' applications and renders them hard to overcome and load in various body areas [2,11]. A nanocomposite polymer hydrogel is a chemically (covalent bond) or physically (non-covalent) cross-linked polymer that inserts nano-sized particles into a matrix of standard material, which also inflates the presence of nanoparticles or nanostructures [12]. Incorporating inorganic nanoparticles with a high surface-to-volume ratio and strength in aqua-gel structure is the most common and effective method for improving their mechanical characteristics [4,13,14]. Various metallic nanoparticles (NPs), including gold, silver (Au, Ag), and metal oxide NPs, such as iron oxide (Fe_3O_4, Fe_2O_3), titania (TiO_2), alumina, and zirconia may be employed to form NC hydrogels for biomedical applications [12]. The well-defined open areas between the gel networks are nanoscopic domains that enable the nanoparticles to develop without aggregating. Nanocomposite hydrogel networks are much more effective in loading metal/metal oxide nanoparticles (magnetite), as they stabilize the particles and prevent oxidation [15]. Various studies revealed nanocomposite hydrogels like Dil et al. [16] reported the antibacterial potential of innovative porous gelatine silver/AcA (NPGESNC-AcA) nanocomposite hydrogels by free radical polymerization. A new drug delivery system of oxidized starch/CuO nanocomposite hydrogels was reported by Gholamali et al. [17], to estimate the cumulative release of drug from metallic nanocomposite hydrogels. Likewise, polyvinyl alcohol/CuO (PVA/CuO) nanocomposite hydrogels also obtained a similar outcome concerning drug delivery potential at pH 7.4 [18]. Katas et al. [19] effectively produced Ag NPs from wasted mushroom substrate (SMS) and incorporated them with genip-incross-linked gelatine hydrogels as wound dressing.

Cancer incidence and microbial drug resistance are the world's leading causes of death. In addition to being a multifactorial illness caused by a mix of hereditary and environmental variables, cancer also contributes to tumour heterogeneity. Chemotherapy, which utilises extremely toxic chemotherapeutic agents against cancer cells, is the recommended way of treatment. It involves delivering anti-cancer drugs intravenously at maximum tolerated dosage, resulting in substantial toxicity to healthy cells, ranging from neutropenia to cardiomyopathy. The quest for viable therapies for numerous cancers is urgent and continuing. Most malignancies, including breast, lung, leukaemia, brain, and lymphoma, respond well to doxorubicin (DOX), commonly known as adriamycin, one of the most widely used anticancer drugs from its family (anthracycline derivatives). However, its high therapeutic effects and clinical applications are hampered by its short half-life, poor bioavailability, and high volume distribution, which necessitate high doses for effective treatment and potentially trigger side effects including cardiotoxicity, extravasation, nephrotoxicity, and myelosuppression. In addition, its effectiveness is diminished by drug resistance ascribed to P-glycoprotein, which may pump DOX out of cells, limiting its intracellular concentration and therapeutic efficiency [20]. There is a need to produce powerful doxorubicin hybrid compounds that can overcome drug resistance with minimised adverse effects [21]. Substantial comorbidities linked with cancer include infections,

osteoporosis, and rheumatoid arthritis (RA), which may be explained in large extent by inflammatory disease process. Symptoms of rheumatoid arthritis frequently include joint discomfort, swelling, and morning joint stiffness. It is an inflammatory disorder that has been linked to lymphomas. Patients with rheumatoid arthritis have an increased risk of cancer, with breast and prostate cancer being the most frequent categories. Cancer development in individuals with arthritis presents substantial therapeutic hurdles and increases the patient's healthcare burden [22]. Therefore, in this study, we successfully fabricated CNC-g-PAA doped CaO NCH by grafting vinyl monomers such as PAA (-COOH) onto the surface of CNCs to enhance its absorption capacity and then added these as dopants on CaO nanoparticles to improve the mechanical property of CNC-g-PAA for efficient drug delivery system. Also, evaluated the potential of copolymerized hydrogel-doped metal oxide for local delivery of doxorubicin against cancer treatment by in vitro cytotoxicity. Furthermore, antibacterial, anti-arthritic effects and molecular docking analysis were conducted to evaluate binding interaction between targeted proteins and synthesized nano-biomaterials (CNC-g-PAA, and CNC-g-PAA doped CaO).

2. Experimental section

2.1. Materials and reagents

Calcium chloride dihydrate ($CaCl_2{\cdot}2H_2O$, 99–101 %), sodium hydroxide (NaOH, 98 %), Poly (acrylic acid), Sodium persulfate ($Na_2S_2O_8$), microcrystalline cellulose Avicel PH101 (~50 μM particle size) were acquired from Sigma-Aldrich (Germany). H_2SO_4 was obtained from Analar (USA).

2.2. Synthesis of cellulose nanocrystals (CNC)

CNC was produced by hydrolyzing Avicel with H_2SO_4 according to described procedure [23,24]. Specifically, 10 g Avicel was hydrolyzed for 30 min at 45 °C in 64 % (*w*/w) H_2SO_4 solution. A substantial volume (1900 mL) of chilled water was used for quenching the reaction to yellow-brown mixture. The further reaction was halted, and suspended particles were allowed to settle overnight at room temperature. The surplus water was decanted and centrifuged (7100 rpm, 12 min) to extract residual cellulose. It was repeatedly rinsed with water until the suspension became transparent, then neutralized by 0.25 M NaOH. The remnant suspension was sonicated for 15 min using a Vibracell Sonicator, and total solid content was measured by drying at 105 °C to attain constant weight. The CNC stock was produced to 97.5 mg/mL concentration and kept at 4 °C till future use.

2.3. Synthesis of CNC-g-PAA

CNC-g-PAA was synthesized using a slightly modified version [25]. Approximately 5 mL of synthesized CNC was added to 75 mL of DI water. The final concentration of CNC was 6.25 mg/mL, which was sonicated for 40 min and degassed under vacuum. Then, 5 mL (13 mg/mL) sodium persulfate solution was introduced as a reaction initiator, and mixture was heated at 50–55 °C for 25 min with constant stirring. Subsequently, drop-by-drop, PAA was added to reaction mixture at a weight ratio of 1:6 (CNC: PAA) within 1 h under incubation at 60–70 °C. After addition, the reaction mixture was incubated for an additional hour. The CNC-g-PAA was harvested by cooling the mixture at room temperature and centrifuging at 7100 rpm for 10 min to decant surplus water. Finally, repeated washing preceded with DI water to remove impurities and unbound polymer, and then sample was lyophilized before storage. Fig. 1 illustrates the chemical structure of CNC-g-PAA.

2.4. Synthesis of CNC-g-PAA doped CaO

A pure colloidal solution of $CaCl_2{\cdot}2H_2O$ (0.5 M) was agitated for 20 min. Subsequently, varying concentrations (2 and 4 wt%) of CNC-g-PAA were introduced to the solution with continuous stirring to achieve a homogeneous solution. To attain pH ~12, NaOH (1 M) prepared solution was incorporated gradually and swirled for 60 min at 80 °C. Centrifugation was employed at 7500 rpm to separate and wash the product. Finally, samples were dried overnight above 100 °C to acquire fine powder [26].

2.5. Characterization of synthesized nanocomposites

2.5.1. Morphology and microstructure of CNC-g-PAA doped CaO

The morphology and microstructural characterization of synthesized samples were analyzed using field-emission scanning electron microscopy (FE-SEM, JSM-6460LV, JEOL, Japan) with energy-dispersive X-ray spectroscopy (EDS, Oxford, UK). The inter-planner d-spacing of fabricated nanomaterials was evaluated with high-resolution transmission electron microscopy (HR-TEM, JEM2100F, JEOL, Japan).

2.5.2. Characterization using X-ray diffraction (XRD), FTIR, DSC, and UV spectrophotometer

XRD patterns of nanomaterials were ascertained with a powder diffractometer (PAN analytical X'pert PRO) and monochromatic Cu Kα radiation (λ ~ 0.0154 nm) to assess the crystalline nature and information related to phase. The samples were scanned at 2θ ambient temperature ranging from 10° to 80°.

The infrared spectra of synthesized materials were acquired using a PerkinElmer attenuated total reflectance-Fourier transform infrared spectroscopy (ATR-FTIR). FTIR spectra were detected by completing 16 scans with a resolution of 500–4000 cm^{-1}. A spectrum of the ambient air was acquired before running each sample.

The 200–800 nm wavelength range of UV–Vis spectrophotometer (Genesys 10S) was used to analyze samples optical properties. Each sample was diluted 10-fold with DI water and mixed well before placing it in a cuvette for analysis.

DSC (model Q2000 V24.11, Build 124) was used to estimate the melting temperature (Tm) of CNC-g-PAA and CNC-g-PAA/CaO. For analysis, 6–10 mg sample was measured in a thermo-aluminum pan with 1 mm diameter hole in the middle of the lid before being set in furnace. The heating scan was initiated from 40 °C to 360 °C with a temperature ramp rate of 20 °C/min in a nitrogenous atmosphere.

2.6. Evaluation of radical scavenging activity:

The radical scavenging activity of synthesized samples was assessed by a modified version of the DPPH assay described previously [27]. In a conventional DPPH scavenging experiment, specimen free radical active species at varying concentrations (10–120 μg/mL) in an equivalent volume of DPPH solution (1 mM) were examined. The reaction mixture was vortexed and incubated in the dark at ambient temperature for 1 h. The ascorbic acid standard solution was utilized as a potent antioxidant reference sample. As stated in Eq. (1), the scavenging content of every sample was calculated via monitoring degradation percentage (%) at an absorbance wavelength of 517 nm.

$$\text{DPPH scavenging rate } (\%) = (C_o - C_t)/C_o * 100 \quad (1)$$

where C_o, absorbance of control sample (methanol + DPPH), and C_t represents absorbance value of synthesized sample after a time interval.

2.7. Anti-arthritic effect of CNC-g-PAA doped CaO on inhibition of protein denaturation by bovine serum albumin (BSA)

The reaction mixture (0.5 mL) comprised 0.45 mL BSA (5 % aq. solution) and 0.05 mL of varied concentrations of CNC-g-PAA doped CaO nanocomposite hydrogel (12.5, 25, 50, 100, 200, 400, 800 μg/mL) respectively. 1 N HCl was used to adjust each solution's pH ~6.3. After

20 min of incubation at 37 °C, the temperature raised to 57 °C for 30 min. Afterwards, 2.5 mL phosphate buffer was incorporated, and absorbance was detected at 660 nm spectrophotometrically. In test control (TC) 0.05 mL distilled water was employed for nanocomposite hydrogel, whereas product control lacked BSA [28]. Using Eq. (2), the denatured protein inhibition was estimated:

$$\%\text{age inhibition} = 100 - (\text{Abs of Test Soln} - \text{Abs of Product Control}/\text{Abs of Control})*100 \quad (2)$$

2.8. Antimicrobial activity

The synthesized CNC, CNC-g-PAA, and CNC-g-PAA/CaO were used to investigate the bactericidal potential using agar-well diffusion assay (AWD) for Gram-positive (*Staphylococcus aureus*) and Gram-negative (*Escherichia coli*) bacteria. *S. aureus* and *E. coli* were effectively recovered from the bovine mastitic fluid by culturing their colonies on Mannitol salt agar (MSA) and MacConkey agar (MA), respectively [29]. For activity, 1.5×10^8 CFU/mL of bacterial strains was wiped on agar plates with 6 mm diameter bores punched by sterile cork borer and filled with two different concentrations (500 and 1000 μg/50 μL) of nanomaterial hydrogels. Alternatively, ciprofloxacin and DI water served as positive and negative controls. Agar plates were incubated at 37 °C for 24 h to cultivate the strains. Then, sensitivity for each sample was assessed by measuring their zone of inhibition with vernier caliper.

2.9. Doxorubicin (DOX) loading on synthesized nanocomposite

The DOX/CNC-g-PAA and DOX/CNC-g-PAA doped CaO were manufactured with modest modifications to the previously published technique [30]. In brief, 1000 μL of 2 mg/mL DOX stock solution was included in a reaction mixture containing 5 mg/mL CNC-g-PAA or CNC-g-PAA/CaO, followed by 20 min of ultrasonication for optimum conjugation of drug with NCHs. The samples were incubated for 24 h using a shaker at ambient temperature in the dark. The pellet was obtained by centrifuging (15,000 rpm for 15 min) the drug-loaded hydrogel nanocomposites. The supernatant was kept in the dark to assess the DOX loading capacity on NCH. The pellet was then lyophilized and retained at 4 °C for future use.

2.10. Determination of loading capacity (LC) and loading efficiency (LE)

As indicated earlier, the supernatant collected following DOX loading was utilized to estimate the amount of unloaded drug by measuring its absorbance at 480 nm via UV–Vis spectroscopy. The concentration of unloaded DOX was estimated using the calibration curve. Then amount of loaded DOX on synthesized NCH was quantified by subtracting unloaded DOX concentration from firstly added DOX. The percentage of LE and LC was derived from Eqs. (3) and (4), respectively.

$$\%\text{Loading Efficiency} = \left[\left(\text{DOX}_i - \text{DOX}_f\right)/\text{DOX}_i\right]*100 \quad (3)$$

$$\text{Loading Capacity}\ \left(\mu\text{g mg}^{-1}\right) = \left[\left(\text{DOX}_i - \text{DOX}_f\right)/\text{Drug}_{\text{carrier}}\right] \quad (4)$$

where, DOX_i and DOX_f showing the initial amount (μg) of added DOX in reaction mixture and unbound DOX in supernatant, respectively. $\text{Drug}_{\text{carrier}}$ display total quantity (mg) of synthesized hydrogels.

2.11. In vitro release of DOX

The DOX release from nanocomposite hydrogel proceeded at two diverse pH values (7.4 and 5.8) in Phosphate buffer saline (PBS). DOX-loaded hydrogel-doped metal oxide was disseminated in 3 mL PBS as a release medium under constant stirring at ambient temperature. At predetermined intervals, 2 mL of release solution was taken and an equal amount of fresh buffer was incorporated into reaction mixture to maintain the sink condition throughout the experiment. The released DOX from nanocomposite hydrogels was assessed using UV–Vis spectroscopy at λ_{max} of drugs. The cumulative DOX release was plotted against time, and proportion of the released drug was approximated using the Eq. (5).

$$\text{Drug Release}\ (\%) = (D_t/D_o)*100 \quad (5)$$

where, D_t is DOX released from nanocomposite hydrogel at a given interval, while D_o is total amount of DOX-loaded on nanocomposite hydrogels [30,31].

2.12. Cell culture and cytotoxicity assessment

The MDA-MB-231 breast cancer cell line was acquired from Centre of Excellence in Molecular Biology, University of the Punjab, Lahore, Punjab, Pakistan, and cultured in a T-75 culture flask in DMEM media along with FBS and antibiotics. The inoculated culture medium was incubated at 37 °C for 24 h in the presence of 5 % CO_2 and 95 % relative humidity. When the culture achieved 80 % confluency, cells were passaged using 0.25 % Trypsin–EDTA after washing with lukewarm PBS^- to remove dead cells, followed by incubation at 37 °C for 4–5 min to detach the cells. The Trypsin–EDTA was made inactive using serum-supplemented media and later cell pellet was extracted by centrifugation (2000 rpm, 10 min) and resuspended in a sterilized fresh medium. For experimentation passage 19 cells were used briefly; 100 μL cells were seeded in 96-well microtiter plate (MTP) containing adjusted cell density (CD) ~10×10^4 and incubated at 37 °C for 24 h under 5 % CO_2. Subsequently, MTT metabolic activity assay was employed to evaluate the cytotoxicity of NCH using MDA-MB-231 cancer cell line. After cultivation, divergent DOX concentrations were used under sterile conditions. For this purpose, 100 μL of 2-fold serial dilution (3.9–500 μL) of CNC-g-PAA and CNC-g-PAA/CaO was poured into 96-well MTP containing fermented cells with fresh culture medium and accomplished incubation at 37 °C for 24 h under 5 % CO_2. The control sample contained 100 % cell viability. The culture medium of fermented MTP was then replenished with 100 μL of fresh PBS, followed by 20 μL of 5 mg/mL MTT solution and incubated for 4 h. Then, fermented medium was substituted with 100 μL DMSO to dissolve formazan crystals and kept in an incubator for 20 min. Finally, an assay reader (ELISA) was used to evaluate absorbance at the wavelength of 500–600 nm [30,32], and calculated percentage viability was using Eq. (6).

$$\text{Cell viability}\ (\%) = (\text{OD of treated cells}/\text{OD of control})*100 \quad (6)$$

2.13. Molecular docking analysis

A molecular docking study was performed to ascertain the molecular activity of CNC-g-PAA and CNC-g-PAA/CaO on various breast cancer receptors. This was attained by focusing on proteins involved in cell development and division. Cyclin-dependent kinase 2 (CDK2), as intriguing target for anti-cancer drugs [33], interacts with phosphorylates proteins in a variety of biological pathways, including DNA destruction, intracellular transport, protein degradation, signal transduction, DNA and RNA metabolism, and translation [34]. CDK2 plays a crucial role in cell cycle regulation and engages in vast array of biological activities. We explored a protein data bank for 3D structure of CDK2 (PDB ID: 2XMY) [35]. SYBYL-X 2.0 was used to perform molecular docking study. The 3D structure was generated using SKETCH module of the software Sybyl-X 2.0 (Fig. S3), accompanied by energy reduction by Tripos force field with Gasteiger Hückel atomic charge [36]. The Surflex-Dock module used to analyze binding interactions of NCH with active site residues of selected proteins, and missing hydrogens were introduced. To enhance atomic charges, the AMBER 7 FF99 force field was employed. Through the Powell method with a convergence gradient of 0.5 kcal/(molA) for 1000 cycles, the energy was dropped to avoid steric conflicts. Every ligand-receptor complex was ranked by an

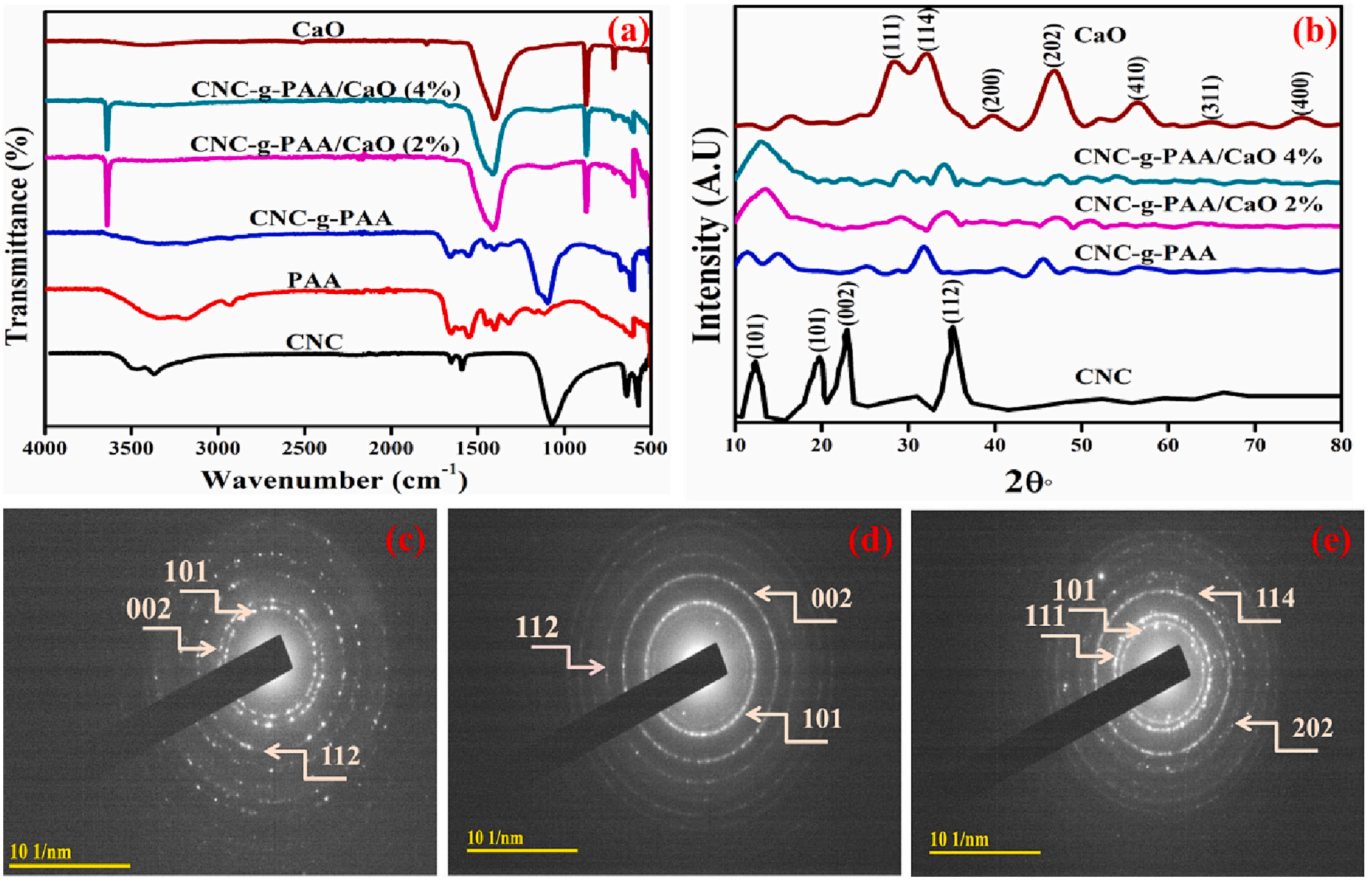

Fig. 2. (a) FTIR spectra, (b) XRD, and (c–e) SAED pattern of CNC, CNC-PAA, and CNC-PAA doped CaO NCH.

empirical consensus scoring (cScore) based on Hammerhead's scoring system [37,38], which consisted entirely of the Chem-Score, crash score, dock-score (D-score), complete score, gold score (G-score), polar score, and potential mean force (PMF) score, using a molecular similarity method (morphological similarity).

2.14. Statistical analysis

GraphPad Prism version 9 used to conduct statistical analysis. All tests were carried out in triplicate, provided mean ± standard deviation (SD) for $n = 3$, and explored using one-way ANOVA. The degree of significance was estimated by p-value. $^{*}p < 0.05$ deemed statistically significant. While, $^{*}p < 0.05$, $^{**}p < 0.007$, and $^{***}p < 0.0005$, $^{****}p < 0.0001$ were considered highly substantial.

3. Results and discussion

3.1. Characterization of synthesized nanocomposite hydrogels

The chemical composition and functional group identification of fabricated nanocomposites were analyzed through FTIR analysis (Fig. 2a). FTIR band nearly 1400 cm^{-1} attributes C—O bond associated with carbonation of CaO nanostructure and peaks at 871 cm^{-1}, and 712 cm^{-1} correspond to Ca—O stretching of nanoparticles [39–41]. In CNC, distinctive peaks were observed at 3000–3600 cm^{-1} (OH stretching) and 1050 cm^{-1} (COC vibration) [42]. While PAA displayed prominent bands at 2951 cm^{-1} (—CH— stretching), 1711–1721 cm^{-1} (C═O stretching), and 1570–1600 cm^{-1} (C═O) peak following oxidation of the carboxylic group [43–45]. Carboxylate (OC═O) presented peaks at 1418 cm^{-1} for symmetrical and asymmetrical stretching vibrations. CNC-g-PAA exhibited similar FTIR spectra with OH, COC, and C═O (COOH) and indicated PAA graft was successfully polymerized onto CNC backbone chains, and all expected peaks, COOH (or —COONa), —OH, —CaO, were seen in CNC-g-PAA/CaO spectra. So, enhanced binding interaction between CaO and CNC-PAA (hydrogel) suggested an increased intensity of peaks at 4 %.

X-ray diffraction in 2θ range of 10°-80° was carried out to explore structural parameters and phase composition of CNC, CNC-g-PAA, and CNC-g-PAA/CaO (2, 4 %), as in Fig. 2b. The diffraction peaks discerned at 2θ = 28.6°, 31.5°, 39.5°, 47.5°, 56.6°, 64.2°, 75.3°, contributed significantly to (111), (114), (200), (102), (202), (410), (311), (400) planes and, verified cubic phase of CaO (JCPDS Card No. 00-037-1497, ICDD Card No. 00-017-0912, JCPDS File No. 37-1497, ICDD Card No 00-003-1123) [46–48]. The major predominant crystalline peaks in CNC sample were identified at 2θ of 12°, 19.5°, 22.4°, and 33.9° [49]. Acid hydrolysis depolymerized cellulose amorphous part, resulting in a crystalline area that remained intact in CNC [50,51]. XRD patterns of CNC-g-PAA displayed substantially all peaks after grafting PAA polymerization with CNC backbone chains, although signal intensity was significantly lowered owing to PAA amorphous pattern [50]. This result showed that CNC was successfully incorporated into PAA via graft polymerization [52]. The peaks get broader with increased doping ion concentration (CNC-g-PAA), which may be ascribed to lattice strain in samples. The nanoscale size of the crystalline sample, strain, and experimental variables may contribute to broadening diffraction peaks [53].

Next, selected area electron diffraction (SAED) analysis label discrete rings pertaining to planes (101), (002), (112), (114), (202), and (111) of both pure (CNC, CNC-g-PAA, CaO) and doped CNC-g-PAA/CaO in Fig. 2 (c–e). These rings corroborated polycrystalline phase of synthesized NCH, and proved that the ring indexing correlated with XRD results to a great extent.

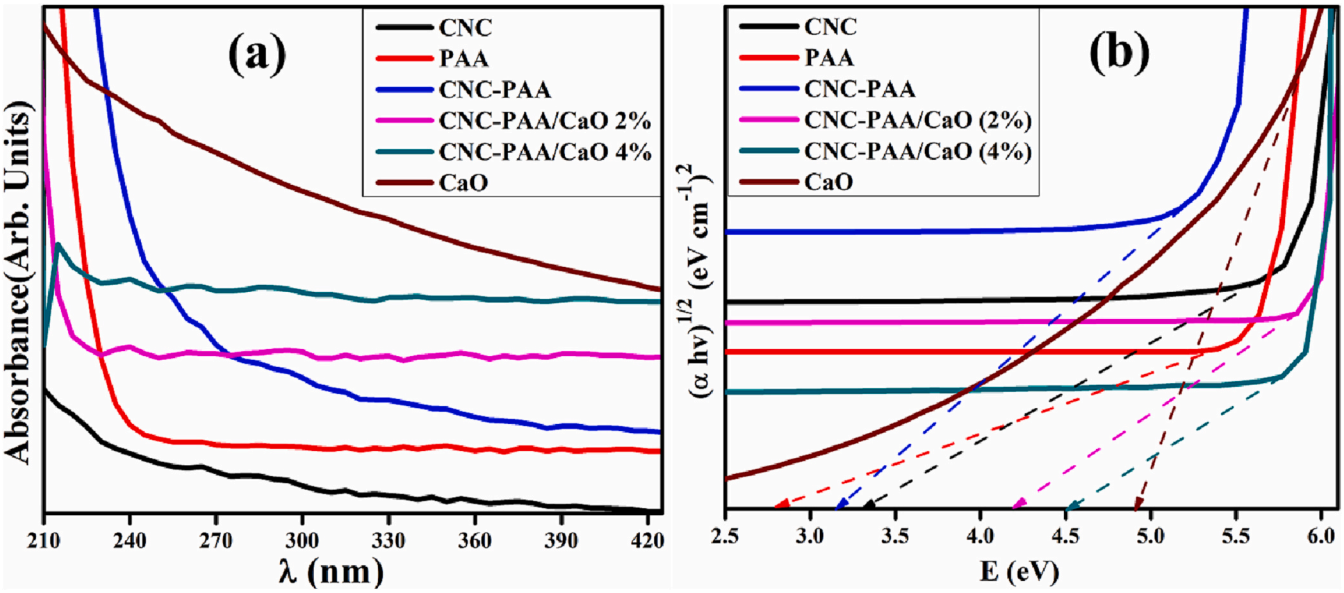

Fig. 3. (a) Absorption spectra (b) Tauc's band gap energy plot

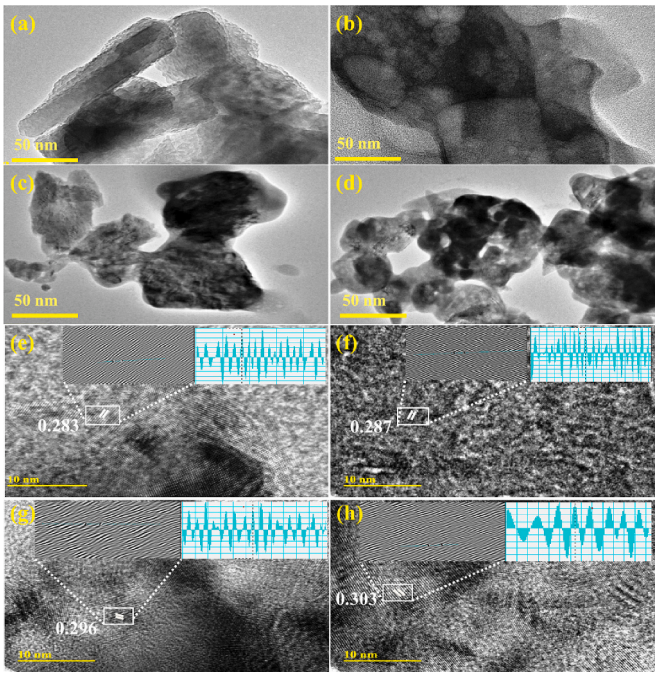

Fig. 4. (a–d) TEM, (e–h) d-spacing of synthesized nanocomposites; (a, e) CNC, (b, f) CNC-g-PAA, (c, g) CNC-g-PAA/CaO (2 %), and (d, h) CNC-g-PAA/CaO (4 %).

UV–Vis spectroscopy was employed to analyze the optical properties and intense band-to-band absorption (Fig. 3a). In wavelength range of 300–800 nm, CNC spectra did not display a noticeable peak [54]. The prominent PAA absorption occurs between 210 and 220 nm; conversely, there is no apparent absorption maxima in longer wavelength ranges [55,56]. The maximum CaO absorption peak was noticed at ~225 and 251 nm UV range [57]. CNC-g-PAA/CaO composites revealed almost comparable absorption bands at 210–270 nm and blue shift toward lower wavelength. Tauc's equation was employed to evaluate band gaps of pure (CNC, PAA) and grafted materials (CNC-g-PAA) as 3.15, 2.1, and 2.9, respectively. Pure CaO exhibited a band gap of around 4.94 eV [58], which was reduced to 4.2 and 4.5 for CNC-g-PAA/CaO (2 % and 4 %). The band energies of CNC-g-PAA/CaO samples declined as crystal size decreased, which could be due to reduced crystallinity and restricted orientation realignment of resultant materials [59] as illustrated in Fig. 3b.

3.2. Size, Surface, and morphology of nanocomposite hydrogel

FESEM was utilized to estimate fabricated samples' surface morphology with negatively charged electrons (Fig. S1 a–d). CNC image revealed non-uniform distribution of crystals in form of rods. The incorporation of CNC-g-PAA into CaO (Fig. S1-c) revealed overlapping of CNC-g-PAA with CaO agglomeration that increased with CNC-g-PAA quantity in metal oxide (Fig. 1-d).

The surface morphology of pure (CNC), grafted (CNC-g-PAA), and doped (CNC-g-PA/CaO 2, 4 %) samples were examined by HR-TEM (Fig. 4 a–d). TEM image exhibited the rod shape of CNC and CNC-g-PAA as highly porous structures. Agglomeration was seen in CNC-g-PAA/CaO (Fig. 4 c, d), attributing to CaO particle's strong interactions at nanoscale [60]. As illustrated in (Fig. 4 e–h), highly magnified interlayer d-spacing of synthesized samples was computed by displaying lattice fringes for crystallographic planes using TEM images (10 nm). The calculated d-spacing for CNC, CNC-g-PAA, and CNC-g-PAA/CaO was ~0.283, 0.287, 0.296, and 0.303 nm, correspondingly, which satisfied the theoretical d-spacing of CaO (2, 4 %), (002, 111) planes (JCPDS File. 01-085-0514).

EDS was used to ascertain the constituent components of pure, grafted, and doped samples (Fig. 5). CaO was successfully integrated into CNC-g-PAA nanocomposites, as shown with the presence of Ca and O peaks. Similarly, peaks in C and O signals indicate the successful incorporation of PAA and CNC into lattice. Furthermore, the presence of Na peak comes from NaOH solution during nanocomposite hydrogel synthesis to adjust the pH. The appearance of extra elements (Au and Cl) may be attributed to EDS detector's high background count.

3.3. Thermoanalytical analysis of NCHs

The thermal behaviour of CNC-g-PAA and successful CNC-g-PAA/CaO (2, 4 %) was investigated using DSC at a temperature ranging from 40 to 350 °C (Fig. 6), with samples processed to 350 °C and then cooled at ambient temperature. The CNC-g-PAA hydrogel thermo-gram displayed two endothermic curves. The first curve at crystalline melting

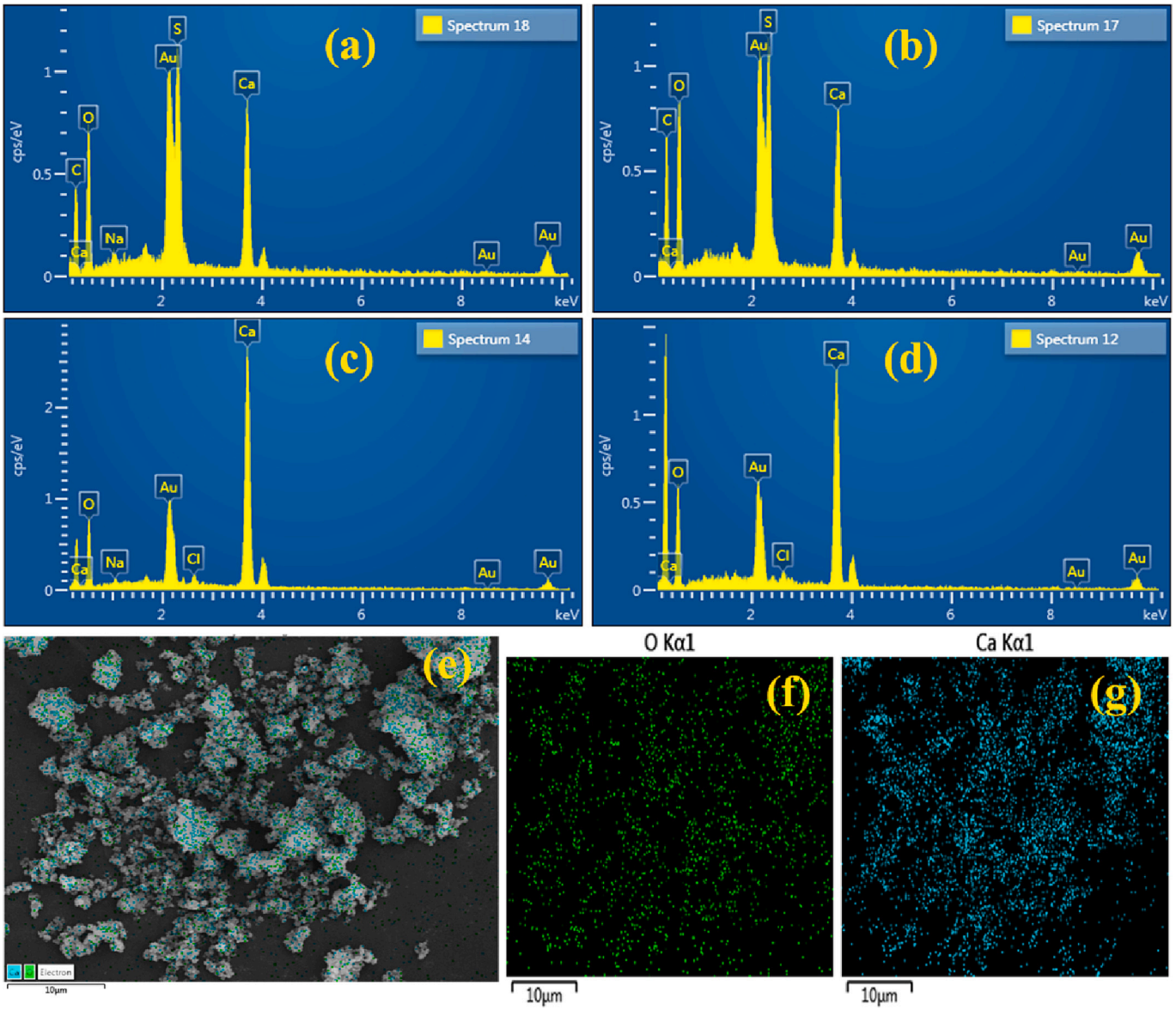

Fig. 5. (a–d) EDS analysis of CNC, CNC-g-PAA, CNC-g-PAA/CaO 2 % and 4 %, (e–g) Elemental mapping of (e) CNC-g-PAA/CaO, (f) O, and (g) Ca.

temperature (Tm) of ~123 °C depicted a phase transition from hard to soft elastic state, comprising water evaporation. At ~275 °C, the second broad curve suggested a breakdown of cross-linking due to polymer disintegration. Whereas glass transition temperature (Tg) of CNC-g-PAA/CaO (2 %) was found near 65 °C and reached 71 °C in CNC-g-PAA/CaO (4 %), followed by a steep endothermic curve at 112 °C temperature. Primarily, mass loss happened below 200 °C owing to hydration of water contents. The exothermic curve at 296 °C in (4 % CNC-g-PAA/CaO) depicts the degradation of CNC-g-PAA/CaO. The sharp endothermic curves represent crystal homogeneity, as crystalline Tm is relatively high, signifying that the structure is more stable and heat resistant [61].

3.4. Free radical scavenging activity

The capacity of a substance to donate electrons or hydrogen atoms toward the DPPH free radical governs its antioxidant properties. Free radical scavenging actions are critical for preventing the detrimental effects of various diseases, including cancer and arthritis [62]. Antioxidants may reduce the oxidative stress in joints, which contributes to the development of arthritis, and they can also maintain more of the body's cells healthy and less likely to develop cancer [63]. Free radical scavenging activity of all produced nanocomposites was evaluated by a dose-dependent pattern (Fig. 7a). CNC-g-PAA doped CaO (4 %) yielded the highest radical scavenging efficiency up to 72.21 % at concentration of 120 μg/mL and scavenged DPPH radicals through their hydrogen donating capability. According to the IC_{50} data, CNC-PAA/CaO (2 and 4 %) revealed IC_{50} values of 94.43 μg/mL and 47.203 μg/mL, respectively (Fig. 7b). The formation of powerful oxidizing •OH and $•O_2$ species may interact with DPPH free radicals and lead to its degradation. These findings revealed that all CNC-g-PAA and CNC-g-PAA doped CaO NCH contained scavenging activity by their electron transfer or hydrogen donating capacity to neutralise radical production, however, scavenging antioxidant activity of NCH was highly correlated with ascorbic acid, used as standard compound [64].

3.5. Anti-arthritic activity

Bovine serum albumin (BSA) was used to assess the inhibitory effects of protein denaturation for CNC, CNC-g-PAA, and CNC-g-PAA-doped CaO (2 % and 4 %) depicted in Fig. 8. Across the concentration ranges (25, 50, 100, 200, and 400 μg/mL), the results exhibited concentration-

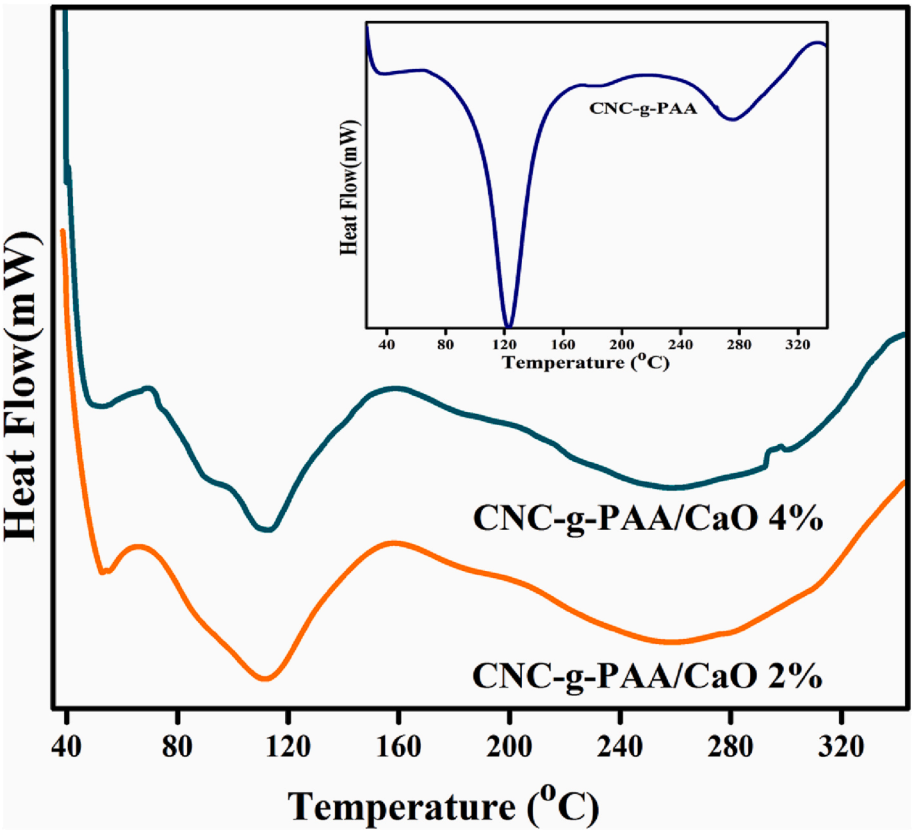

Fig. 6. DSC spectra of CNC-g-PAA and CNC-g-PAA/CaO (2 % and 4 %).

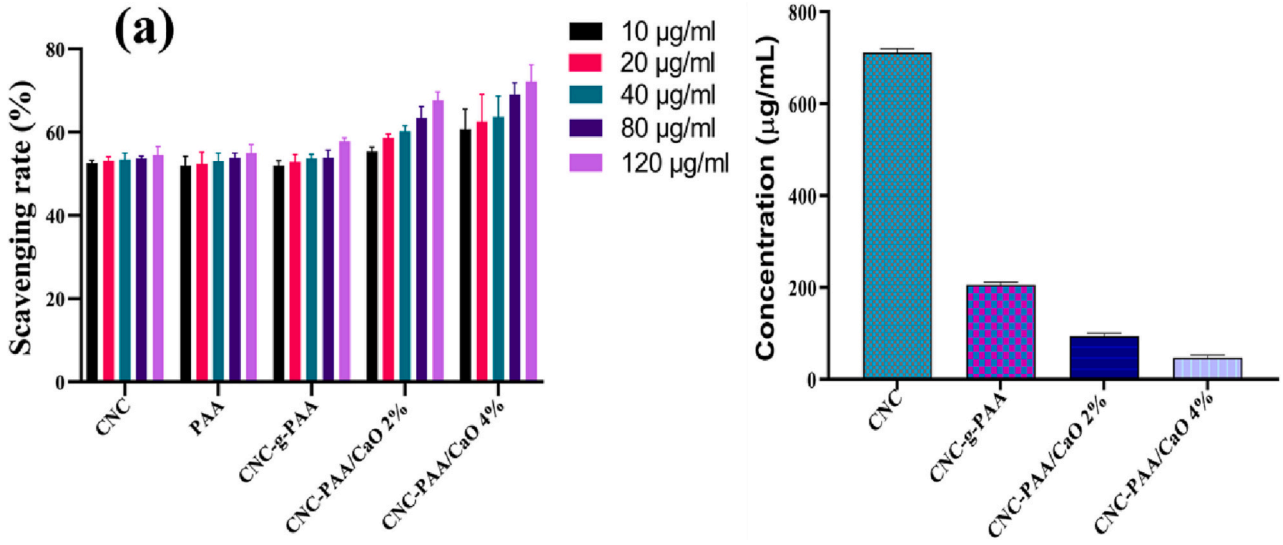

Fig. 7. (a) DPPH radical scavenging potential (b) IC_{50} of synthesized samples.

dependent attenuation of protein denaturation by NCH. At 400 µg/mL, CNC-g-PAA/CaO (2 %) inhibited protein denaturation by 59.41 % in contrast to CNC-g-PAA/CaO (4 %) as 71.13 %. It was observed that antioxidants could also function as anti-inflammatory agents [65]. It is generally acknowledged that reactive oxygen species (ROS) stimulate many intracellular signalling pathways, therefore triggering numerous pro-inflammatory cytokines. ROS also function as secondary messengers and stimulate other inflammatory mediators [66]. By modulating cell signalling and gene expression, these components (CNC-g-PAA/CaO) reduce the formation of inflammatory mediators and oxidants [67].

3.6. Anti-microbial evaluation

The in-vitro bactericidal efficiency for CNC, CNC-g-PAA, and CNC-g-PAA doped CaO (2, 4 %) against *E. coli* and *S. aureus* was evaluated by measuring inhibition regions (mm) diameter using well diffusion technique depicted in Table 1. CNC, PAA, and CNC-g-PAA presented null efficacy against both bacterial isolates at least concentrations. Significant inhibition areas ($p < 0.05$) for *E. coli* were detected (0.55–4.75 mm) and (1.05–6.05 mm), respectively, and (4.25–5.05 mm) for *S. aureus* at maximal concentrations (1000 µg/50 µL) however, (1.90–2.80 mm) was

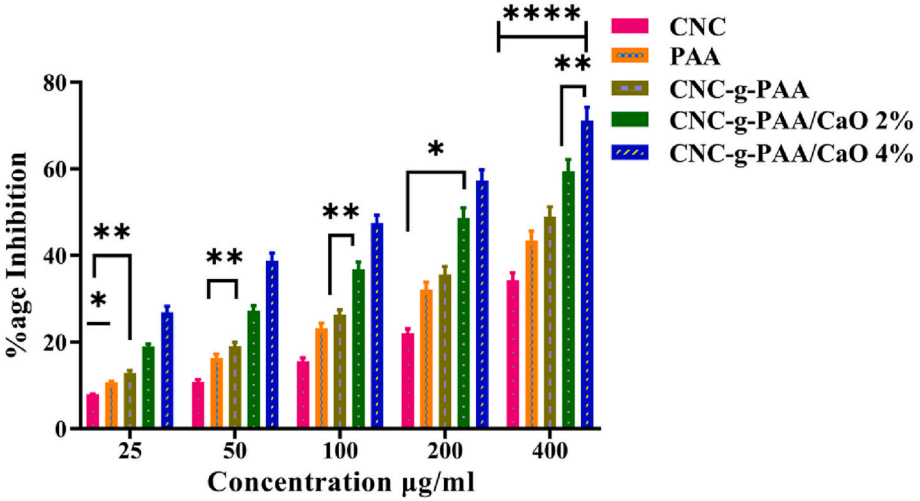

Fig. 8. Effect of CNC, CNC-g-PAA, CNC-g-PAA/CaO (2, 4 %) on the inactivation of protein employing bovine serum albumin. Every values presented as mean ± S·D ($n = 3$), using one-way ANOVA. **** = $p < 0.0001$, ** = $p < 0.001$, * = $p < 0.05$.

Table 1
Antimicrobial activity of NCH.

Sample	Inhibition zones (mm) of *S. aureus*		Inhibition zones (mm) of *E. coli*	
	500 µg/50 µL	1000 µg/50 µL	500 µg/50 µL	1000 µg/50 µL
CNC	0	0.35	0	0
PAA	0	0.90	0	0
CNC-g-PAA	0	1.10	0.55	1.05
CNC-g-PAA/CaO (2 %)	1.90	4.25	3.95	5.45
CNC-g-PAA/CaO (4 %)	2.80	5.05	4.75	6.05
Ciprofloxacin	6.50	6.50	7.15	7.15
DI water	0	0	0	0

recorded at minimal (500 µg/50 µL) concentration for doped NCH. DIW (0 mm) as negative and ciprofloxacin (6.50 and 7.15 mm) as positive control were used to compare *E. coli* and *S. aureus* inhibition regions. NCH antibacterial activity can be attributed to numerous phenomena, such as electrostatic interactions with OH^- and H_2O fascinated at the surface, resulting in reactive oxygen species (ROS) production. Primarily, a reaction between cations Ca^{2+} and negatively charged regions of collapsing bacterial cells causes electronic excitation of CaO valance band surfaces upon irradiation, resulting in a bactericidal effect. Additional O_2 reactions yield O^{-2} radicals, leading to the production of H_2O_2. The resultant O^{-2} species play crucial functions in the breakdown of lipid or protein molecules on the bacteria's outer cell surface [68]. Due to variations in bacterial membrane structure, CNC-g-PAA/CaO (4 %) showed considerable antibacterial efficacy against *E. coli* in contrast with *S. aureus*.

3.7. DOX loading and releasing efficiency

DOX was entrapped in synthesized hydrogels (CNC-g-PAA and CNC-g-PAA/CaO (2, 4 %)) by electrostatic interaction between the positive and negative charges of DOX and –CaO-based NCH, respectively. In the UV–vis range (Fig. 9a), the distinct absorption bands of free DOX versus DOX-loaded samples are apparent. Free DOX exhibited a strong absorption band at 482 nm, also detected in produced NCH. After loading hydrophilic drug on NCH, the absorption band of DOX-loaded NCH showed maximum loading into (CNC-g-PAA/CaO 4 %) as 99.31 %. Releasing of DOX from CNC-g-PAA/CaO NCH was found at 480 nm. A strong binding interaction of DOX with CNC-g-PAA/CaO complex could be potentially helpful in preventing premature drug release prior to its target location [69]. The predicted LE values of DOX for CNC-g-PAA and

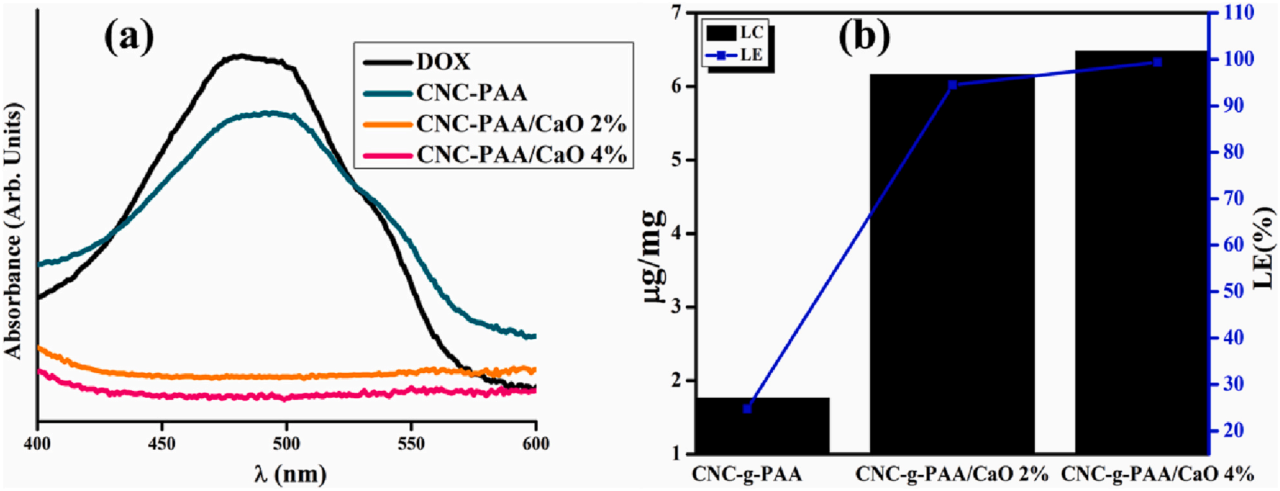

Fig. 9. (a) UV–vis spectra-based drug loading profile of DOX into NCH (b) LC and LE of loaded drug.

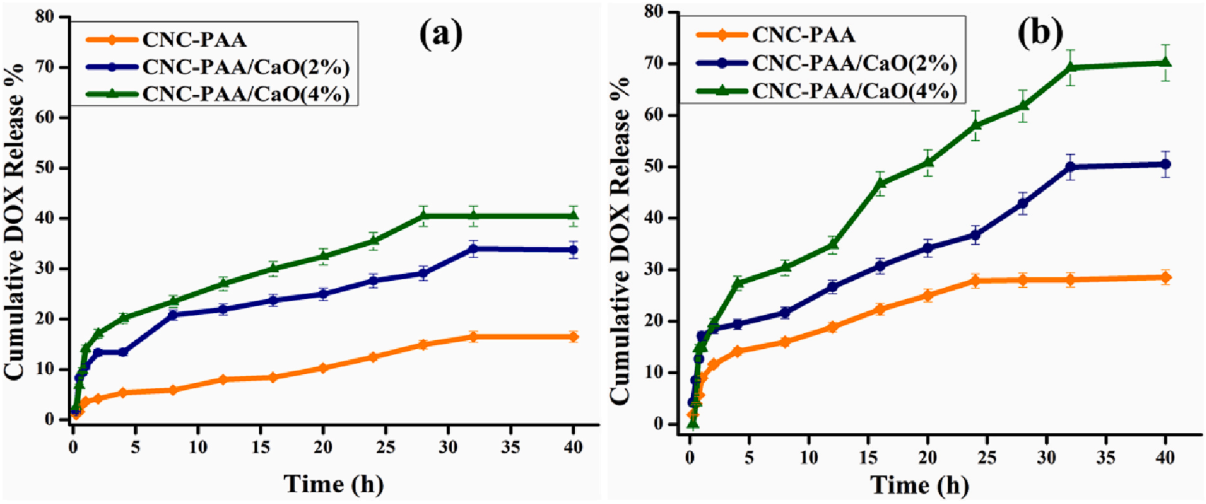

Fig. 10. DOX release behaviour from drug loaded samples (CNC-g-PAA), CNC-g-PAA/CaO (2 %), CNC-g-PAA/CaO (4 %) at (a) pH 7.4 and (b) pH 5.8. Shown values are means ± standard deviation ($n = 3$).

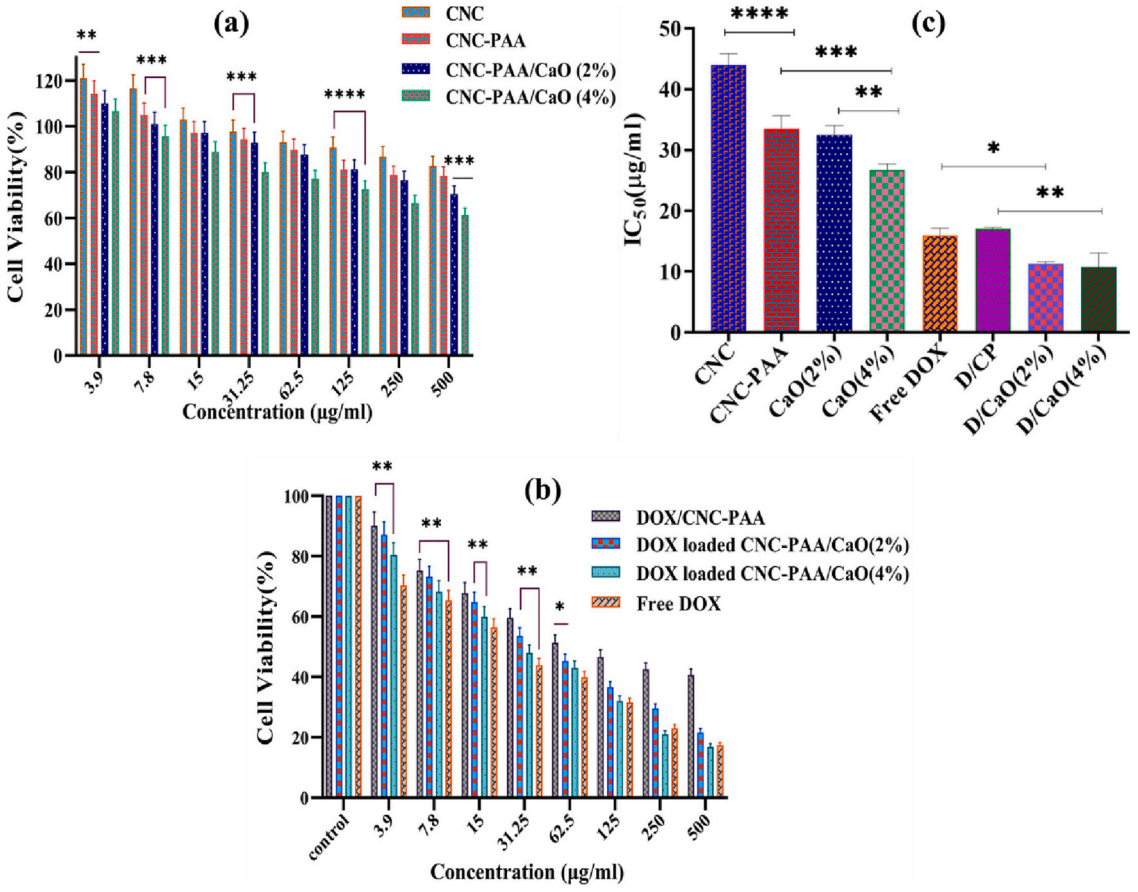

Fig. 11. (a) Viability of MDA-MB-231 cells determined at different concentrations of the drug-free nanocomposite (b) Cell viability of MDA-MB-231cells cells after exposure to diverse doses of drug-loaded hydrogel, DOX/CNC-g-PAA, and DOX/CNC-g-PAA/CaO. (c) The IC_{50} comparison of the various drug formulations. Error bars depict the standard deviation of three independent trials. One-way ANOVA was used to compare various groups, $^{*}p < 0.05$, $^{**}p < 0.007$, $^{***}p < 0.0005$, $^{****}p < 0.0001$.

CNC-g-PAA/CaO (2 and 4 %) were 24.75, 94.48, and 99.35 %, accordingly (Fig. 9b). LC of the grafted sample, on the other hand, was 1.76 µg mg^{-1}, while for doped NCH 6.16 and 6.48 µg mg^{-1} revealed considerably higher LC and LE values in doped sample (CNC-g-PAA/CaO) than CNC-g-PAA.

The pH-triggered based DOX release from DOX-loaded NCH was evaluated using PBS having two different conditions (pH 7.4 and 5.8), chosen correspondingly to provide mimic neutral and mild acidic environments for healthy and intratumoral cells (endosomes). Consequently, the releasing rate of DOX was significantly lower for pH 7.4 in contrast to pH 5.8, as seen in Fig. 10. Regarding the DOX releasing efficiency, CNC-g-PAA/CaO (4 %) exhibited a higher release rate

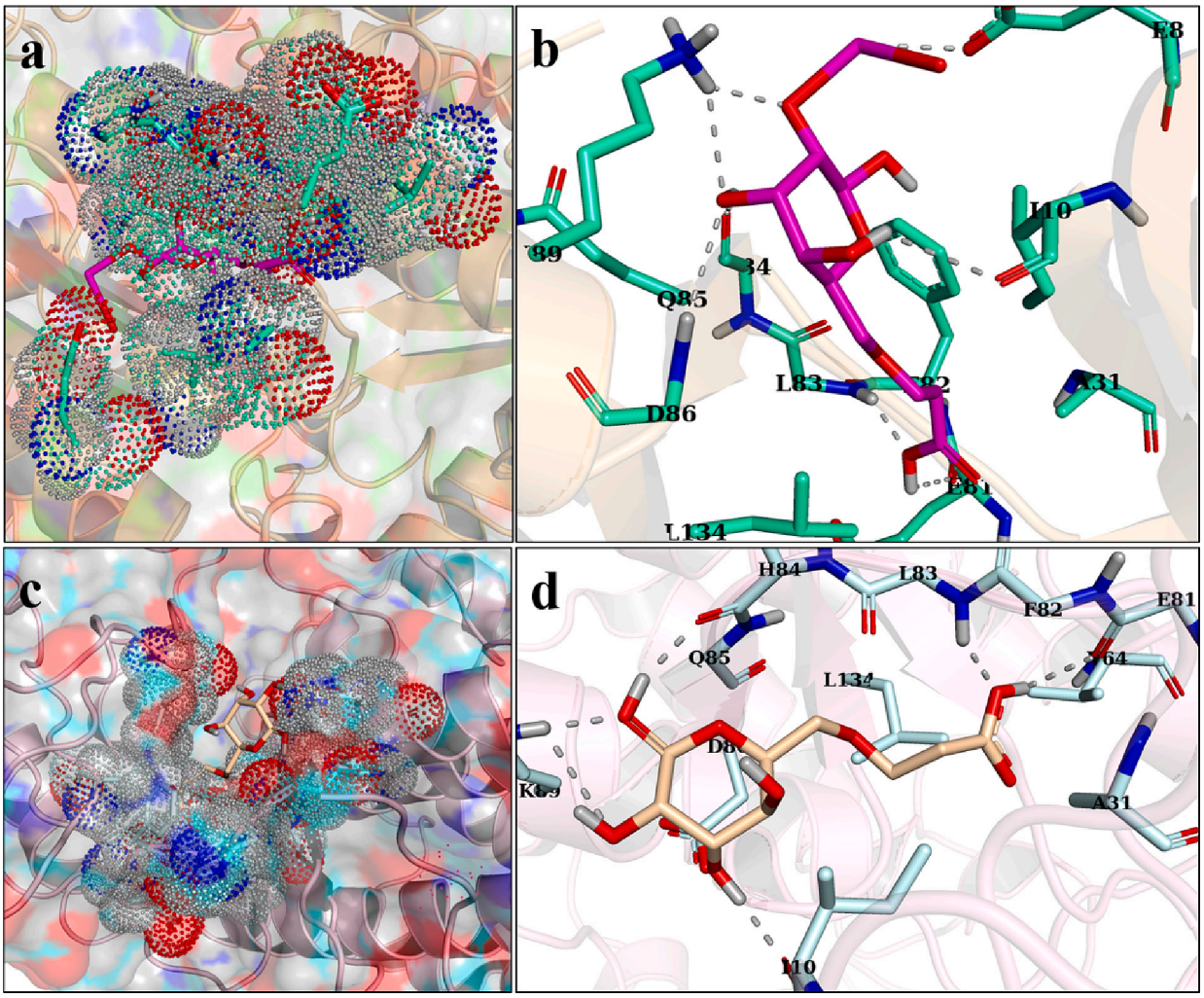

Fig. 12. (a), (b) Binding site and binding interaction pattern of CNC-g-PAA/CaO inside CDK2; (c), (d) Binding site and binding interaction pattern of CNC-g-PAA.

compared to CNC-g-PAA/CaO (2 %) and CNC-g-PAA. Under neutral conditions (pH 7.4), DOX loaded CNC-g-PAA/CaO (4 %) hydrogel released drug merely up to 14.13 % within the first hour and < 40 % after 24 h Fig. 10(a). In comparison, the system revealed a relatively rapid drug release rate in slightly acidic environment (pH 5.8), as shown in Fig. 10(b). Initially observed rate of released DOX was around 14.83 % and increased to 70.19 % when the period was extended to >24 h, which was relatively higher than pH 7.4. DOX releasing from NC hydrogels under mild acidic conditions contribute toward enhanced drug hydrophilicity by increased protonated amine groups and reduced electrostatic interactions. However, strong electrostatic interaction between positively charged DOX molecules and negatively charged —COOH will impede DOX release from hydrogel at pH 7.4. DOX was first released from hydrophobic core area of polymeric nanocomposite, then diffused out of hydrophilic outer shell, and finally entered the incubation medium. This release demonstrates utility of NCH as potent drug carrier that minimises the exposure of healthy tissues while increasing accumulation of therapeutic drugs at the tumour site, thereby eliminating the need for recurrent DOX therapy, the major cause of cardiotoxicity. So, NCH could be stable carriers for targeted drug delivery with minimal leakage through blood circulation (pH 7.4); conversely, a significant amount of drug released at moderately acidic pH as in intratumoral cells of lysosomes (pH 4–5) and endosomes (pH 5–6).

3.8. *In vitro cytotoxicity and in silico analysis*

The MTT assay was conducted on MDA-MB-231 breast cancer cells for 24 h to evaluate the biocompatibility and anti-tumour potential of DOX and CaO-based NCH. The dose-dependent potential of cells treated with unloaded and loaded NCH were assessed between concentration ranges (3.9–500 μg/mL) as shown in Fig. 11(a, b). The cytotoxic action of drug-loaded nanocomposites, found to be greater than unloaded composites, implied the potential of nanocarriers to improve drug uptake through an endocytic mechanism coupled with the reduction in cancer cells' survival. As depicted in Fig. 11c, the amount of IC_{50} for nanocarriers was much lower than free and unbound drug nanocomposites (NCH), representing the enhanced cytotoxic effect DOX in combination with each other. The IC50 amount of nanocomposites in MDA-MB-231 cells was 33.70 and 26.31 μg/mL of CNC-PAA/CaO (2 % ad 4 %), while when the cells were treated with NCH along with DOX, it decreased to 11.63 and 10.7 μg/mL, respectively. The findings suggest that CNC-g-PAA/CaO could enhance therapeutic effectiveness of cancerous drug DOX by binding with DNA through intercalation and triggering a cascade of biochemical reactions causing apoptotic cell death. After 24 h of treatment, cell proliferation of varied drug concentrations revealed a substantial dose-dependent pattern. CNC-g-PAA and its composites act as an agonist in conjunction with the chemotherapeutic drug DOX to achieve a synergetic impact against MDA-MB-231 cancer cells. The simultaneous DOX and CNC-g-PAA released after internalization and amplified accumulation toward the tumour site may

account for improved cytotoxicity [70]. According to in vitro cytotoxicity experiments, the DOX and CNC-g-PAA/CaO formulation exhibited synergistic effectiveness and enhanced cytotoxicity than CNC-g-PAA hydrogel [25].

The use of in silico molecular docking studies in determining the probable mechanism behind diverse biological activities is well recognized. The docking score, as well as interaction pattern within the active pocket of CDK2 enzyme, revealed CNC-g-PAA and CNC-g-PAA/CaO NCH as prospective inhibitors of this enzyme. For CDK2 enzyme, optimal docked conformation reported for CNC-g-PAA exhibited H-bonding interactions with E81, L83, H84, K89, and I10 with a binding score of 5.34 (Fig. 12c and d), whereas CNC-g-PAA/CaO displayed a metal-contact interaction with L83 in addition to H-bonding interactions with E81, L83, H84, K89, and I10 (Fig. 12a and b) and 6.70 overall cumulative binding score.

4. Conclusion

A novel hydrogel doped metal oxide (CNC-g-PAA/CaO) was successfully fabricated and evaluated for bactericidal, arthritic activities and controlled drug delivery. FTIR, XRD, and TGA were used to investigate the chemical composition and heat stability of synthesized NCH. Morphological analysis revealed that generated CNC from crystalline cellulose by strong acid hydrolysis retained rod-shaped structures, and CNC-g-PAA presented porous sponge-like morphology. UV–vis absorptions spectroscopy reported decrease in band gap after addition of CNC-g-PAA into CaO. The free radical scavenging activity-based results confirmed CNC-g-PAA/CaO (4 %) highest scavenging performance up to 72.21 %. The inflammatory potential of samples was found to be comparable with standard (diclofenac sodium). NCHs revealed significant bactericidal efficiency against gram-negative bacteria. After this, these negatively charged hydrogels effectively entrapped hydrophilic drug DOX with positive charges by electrostatic interactions with LE of 99.3 %. In vitro release behaviour from DOX-loaded nanocomposite hydrogels revealed an adequate, stable, and controlled release at pH 5.8. Finally, in vitro cytotoxicity study illustrated the synergistic effect of DOX and CNC-g-PAA/CaO to induce apoptosis in breast cancer cells (MDA-MB-231). In silico analysis for validation of cytotoxicity mechanism revealed these NCH as potent inhibitor of CDK2. Based on these findings, CNC-g-PAA/CaO hydrogels are viable candidates for targeted and controlled release of the hydrophilic drug.

CRediT authorship contribution statement

Iram Shahzadi, Investigation, Writing original draft
Muhammad Islam, Supervision, Data Curation and writing
Hamid Saeed, Supervision, Review and Editing
Anum Shahzadi, Software and Formal Analysis
Junaid Haider, Software and Formal Analysis
Ali Haider, Methodology and Writing
Muhammad Imran, Review and Editing
Hassaan Anwer Rathore-Supervision, Review and Editing
Anwar Ul-Hamid, Resources and Review and Editing
Walid Nabgan, Review and Editing
Muhammad Ikram, Conceptualization and Project administration

Declaration of competing interest

No known conflict of interest.

Data availability

Data available on proper request.

Acknowledgements

Authors are gratified to Higher Education Commission (HEC) Pakistan, through NRPU project-20-17615 (Dr. Muhammad Ikram).

Appendix A. Supplementary data

Supplementary data to this article can be found online at https://doi.org/10.1016/j.ijbiomac.2023.123874.

References

[1] K. Park, Controlled drug delivery systems: past forward and future back, J. Control. Release 190 (2014) 3–8, https://doi.org/10.1016/J.JCONREL.2014.03.054.
[2] S. Rafieian, H. Mirzadeh, H. Mahdavi, M.E. Masoumi, A review on nanocomposite hydrogels and their biomedical applications, Sci. Eng. Compos. Mater. 26 (2019) 154–174, https://doi.org/10.1515/secm-2017-0161.
[3] S. Merino, C. Martín, K. Kostarelos, M. Prato, E. Vázquez, Nanocomposite hydrogels: 3D polymer-nanoparticle synergies for on-demand drug delivery, ACS Nano 9 (2015) 4686–4697, https://doi.org/10.1021/acsnano.5b01433.
[4] A.K. Gaharwar, N.A. Peppas, A. Khademhosseini, Nanocomposite hydrogels for biomedical applications, Biotechnol. Bioeng. 111 (2014) 441–453, https://doi.org/10.1002/BIT.25160.
[5] P. Yin, Hydrogel-based Nanocomposites And Laser-assisted Surface Modification for Biomedical Application, Thesis Diss. Repos, Univ. West. Ontario - Electron, 2012. https://ir.lib.uwo.ca/etd/879 (accessed April 26, 2022).
[6] M. Mahinroosta, Z. Jomeh Farsangi, A. Allahverdi, Z. Shakoori, Hydrogels as intelligent materials: a brief review of synthesis, properties and applications, Mater. Today Chem. 8 (2018) 42–55, https://doi.org/10.1016/J.MTCHEM.2018.02.004.
[7] M. Bahram, N. Mohseni, M. Moghtader, An introduction to hydrogels and some recent applications, in: Emerg. Concepts Anal. Appl. Hydrogels, 2016, https://doi.org/10.5772/64301.
[8] D. Seliktar, Designing cell-compatible hydrogels for biomedical applications, Science (80-.) 336 (2012) 1124–1128, https://doi.org/10.1126/science.1214804.
[9] A. Mohandas, P.T. Sudheesh Kumar, B. Raja, V.K. Lakshmanan, R. Jayakumar, Exploration of alginate hydrogel/nano zinc oxide composite bandages for infected wounds, Int. J. Nanomedicine 10 (2015) 53, https://doi.org/10.2147/IJN.S79981.
[10] S. Utech, A.R. Boccaccini, A review of hydrogel-based composites for biomedical applications: enhancement of hydrogel properties by addition of rigid inorganic fillers, J. Mater. Sci. 51 (2016) 271–310, https://doi.org/10.1007/s10853-015-9382-5.
[11] H.S. Song, O.S. Kwon, J.-H. Kim, J. Conde, N. Artzi, 3D hydrogel scaffold doped with 2D graphene materials for biosensors and bioelectronics, Biosens. Bioelectron. 89 (2017) 187–200, https://doi.org/10.1016/j.bios.2016.03.045.
[12] P. Schexnailder, G. Schmidt, Nanocomposite polymer hydrogels, Colloid Polym. Sci. 287 (2009) 1–11, https://doi.org/10.1007/s00396-008-1949-0.
[13] N. Moini, A. Jahandideh, G. Anderson, Inorganic nanocomposite hydrogels: present knowledge and future challenge, in: Sustain. Polym. Compos. Nanocomposites, 2019, pp. 805–853, https://doi.org/10.1007/978-3-030-05399-4_28.
[14] Y. Sasaki, K. Akiyoshi, Nanogel engineering for new nanobiomaterials: from chaperoning engineering to biomedical applications, Chem. Rec. 10 (2010) 366–376, https://doi.org/10.1002/TCR.201000008.
[15] J. Zhang, S. Xu, E. Kumacheva, Polymer microgels: reactors for semiconductor, metal, and magnetic nanoparticles, J. Am. Chem. Soc. 126 (2004) 7908–7914, https://doi.org/10.1021/ja031523k.
[16] N.N. Dil, M. Sadeghi, Free radical synthesis of nanosilver/gelatin-poly (acrylic acid) nanocomposite hydrogels employed for antibacterial activity and removal of Cu(II) metal ions, J. Hazard. Mater. 351 (2018) 38–53, https://doi.org/10.1016/j.jhazmat.2018.02.017.
[17] I. Gholamali, S.N. Hosseini, E. Alipour, M. Yadollahi, Preparation and characterization of oxidized Starch/CuO nanocomposite hydrogels applicable in a drug delivery system, Starch-Stärke 71 (2019), 1800118, https://doi.org/10.1002/STAR.201800118.
[18] Y. Ahmadian, A. Bakravi, H. Hashemi, H. Namazi, Synthesis of polyvinyl alcohol/CuO nanocomposite hydrogel and its application as drug delivery agent, Polym. Bull. 76 (2019) 1967–1983, https://doi.org/10.1007/s00289-018-2477-9.
[19] H. Katas, M.A.Mohd Akhmar, S.Suleman Ismail Abdalla, in: Biosynthesized silver nanoparticles loaded in gelatine hydrogel for a natural antibacterial and anti-biofilm wound dressing 36, 2021, pp. 111–123, https://doi.org/10.1177/0883911520988303.
[20] A. Fahmi, M. Abdur-Rahman, O. Mahareek, M.A. Shemis, Synthesis, characterization, and cytotoxicity of doxorubicin-loaded polycaprolactone nanocapsules as controlled anti-hepatocellular carcinoma drug release system, BMC Chem. 16 (2022) 95, https://doi.org/10.1186/s13065-022-00888-w.
[21] S. Peter, S. Alven, R.B. Maseko, B.A. Aderibigbe, Doxorubicin-based hybrid compounds as potential anticancer agents: a review, Molecules 27 (2022) 4478, https://doi.org/10.3390/molecules27144478.
[22] B. Bhandari, B. Basyal, M.S. Sarao, V. Nookala, Y. Thein, Prevalence of cancer in rheumatoid arthritis: epidemiological study based on the National Health and

Nutrition Examination Survey (NHANES), Cureus 12 (2020), https://doi.org/10.7759/cureus.7870.
[23] E. Lizundia, U. Goikuria, J.L. Vilas, F. Cristofaro, G. Bruni, E. Fortunati, I. Armentano, L. Visai, L. Torre, Metal nanoparticles embedded in cellulose nanocrystal based films: material properties and post-use analysis, Biomacromolecules 19 (2018) 2618–2628, https://doi.org/10.1021/ACS.BIOMAC.8B00243/SUPPL_FILE/BM8B00243_SI_001.PDF.
[24] J. Nsor-Atindana, H. Douglas Goff, W. Liu, M. Chen, F. Zhong, The resilience of nanocrystalline cellulose viscosity to simulated digestive processes and its influence on glucose diffusion, Carbohydr. Polym. 200 (2018) 436–445, https://doi.org/10.1016/j.carbpol.2018.07.088.
[25] M.R. Vakili, W. Mohammed-Saeid, A. Aljasser, J. Hopwood-Raja, B. Ahvazi, Y. Hrynets, M. Betti, A. Lavasanifar, Development of mucoadhesive hydrogels based on polyacrylic acid grafted cellulose nanocrystals for local cisplatin delivery, Carbohydr. Polym. 255 (2021), 117332, https://doi.org/10.1016/j.carbpol.2020.117332.
[26] M. Ikram, A. Mahmood, A. Haider, S. Naz, A. Ul-Hamid, W. Nabgan, I. Shahzadi, J. Haider, I. Ahmad, S. Ali, Dye degradation, antibacterial and in-silico analysis of Mg/cellulose-doped ZnO nanoparticles, Int. J. Biol. Macromol. 185 (2021) 153–164, https://doi.org/10.1016/j.ijbiomac.2021.06.101.
[27] S.O.Ali Ahmad, M. Ikram, M. Imran, S. Naz, A. Ul-Hamid, A. Haider, A. Shahzadi, J. Haider, Novel prism shaped C 3 N 4 -doped Fe@Co 3 O 4 nanocomposites and their dye degradation and bactericidal potential with molecular docking study, RSC Adv. 11 (2021) 23330–23344, https://doi.org/10.1039/D1RA03949K.
[28] Alamgeer, A.M. Uttra, U.H. Hasan, Anti-arthritic activity of aqueous-methanolic extract and various fractions of Berberis orthobotrys Bien ex Aitch, BMC Complement. Altern. Med. 17 (2017) 371, https://doi.org/10.1186/s12906-017-1879-9.
[29] A. Ul-Hamid, H. Dafalla, A.S. Hakeem, A. Haider, M. Ikram, In-vitro catalytic and antibacterial potential of green synthesized CuO nanoparticles against prevalent multiple drug resistant bovine mastitogen Staphylococcus aureus, Int. J. Mol. Sci. 23 (2022), https://doi.org/10.3390/IJMS23042335.
[30] F. Abedi, S. Davaran, M. Hekmati, A. Akbarzadeh, B. Baradaran, S.V. Moghaddam, An improved method in fabrication of smart dual-responsive nanogels for controlled release of doxorubicin and curcumin in HT-29 colon cancer cells, J. Nanobiotechnol. 19 (2021) 18, https://doi.org/10.1186/s12951-020-00764-6.
[31] H. Afzal, M. Ikram, S. Ali, A. Shahzadi, M. Aqeel, A. Haider, M. Imran, S. Ali, Enhanced drug efficiency of doped ZnO–GO (graphene oxide) nanocomposites, a new gateway in drug delivery systems (DDSs), Mater. Res. Express 7 (2020), 015405, https://doi.org/10.1088/2053-1591/ab61ae.
[32] S. Liaqat, M. Islam, H. Saeed, M. Iqtedar, A. Mehmood, Investigation of Olea ferruginea Roylebark extracts for potential in vitro antidiabetic and anticancer effects, Turk.J. Chem. 45 (2021) 92–103, https://doi.org/10.3906/kim-2006-51.
[33] T.A. Chohan, J.-J. Chen, H.-Y. Qian, Y.-L. Pan, J.-Z. Chen, Molecular modeling studies to characterize N-phenylpyrimidin-2-amine selectivity for CDK2 and CDK4 through 3D-QSAR and molecular dynamics simulations, Mol. BioSyst. 12 (2016) 1250–1268, https://doi.org/10.1039/C5MB00860C.
[34] H.O. Rasul, B.K. Aziz, D.D. Ghafour, A. Kivrak, In silico molecular docking and dynamic simulation of eugenol compounds against breast cancer, J. Mol. Model. 28 (2022) 17, https://doi.org/10.1007/s00894-021-05010-w.
[35] S. Wang, G. Griffiths, C.A. Midgley, A.L. Barnett, M. Cooper, J. Grabarek, L. Ingram, W. Jackson, G. Kontopidis, S.J. McClue, C. McInnes, J. McLachlan, C. Meades, M. Mezna, I. Stuart, M.P. Thomas, D.I. Zheleva, D.P. Lane, R.C. Jackson, D.M. Glover, D.G. Blake, P.M. Fischer, Discovery and characterization of 2-Anilino-4- (thiazol-5-yl)pyrimidine transcriptional CDK inhibitors as anticancer agents, Chem. Biol. 17 (2010) 1111–1121, https://doi.org/10.1016/j.chembiol.2010.07.016.
[36] M. Clark, R.D. Cramer, N. Van Opdenbosch, Validation of the general purpose tripos 5.2 force field, J. Comput. Chem. 10 (1989) 982–1012, https://doi.org/10.1002/jcc.540100804.
[37] W. Welch, J. Ruppert, A.N. Jain, Hammerhead: fast, fully automated docking of flexible ligands to protein binding sites, Chem. Biol. 3 (1996) 449–462, https://doi.org/10.1016/S1074-5521(96)90093-9.
[38] A.N. Jain, Scoring noncovalent protein-ligand interactions: a continuous differentiable function tuned to compute binding affinities, J. Comput. Aided Mol. Des. 10 (1996) 427–440, https://doi.org/10.1007/BF00124474.
[39] P. Raizada, P. Shandilya, P. Singh, P. Thakur, Solar light-facilitated oxytetracycline removal from the aqueous phase utilizing a H 2 O 2/ZnWO 4/CaO catalytic system, J. Taibah Univ. Sci. 11 (2017) 689–699, https://doi.org/10.1016/j.jtusci.2016.06.004.
[40] A. Roy, J. Bhattacharya, Microwave-assisted synthesis and characterization of CaO nanoparticles, Int. J. Nanosci. 10 (2011) 413–418, https://doi.org/10.1142/S0219581X11008150.
[41] V. Sumathi, Optical characterization of calcium oxide nanoparticles, Int. J. Adv. Technol. Eng. Sci. 5 (2017) 63–67.
[42] M. Ikram, S. Hayat, M. Imran, A. Haider, S. Naz, A. Ul-Hamid, I. Shahzadi, J. Haider, A. Shahzadi, W. Nabgan, S. Ali, Novel Ag/cellulose-doped CeO2 quantum dots for efficient dye degradation and bactericidal activity with molecular docking study, Carbohydr. Polym. 269 (2021), 118346, https://doi.org/10.1016/j.carbpol.2021.118346.
[43] W.-M. Cheng, X.-M. Hu, Y.-Y. Zhao, M.-Y. Wu, Z.-X. Hu, X.-T. Yu, Preparation and swelling properties of poly(acrylic acid-co-acrylamide) composite hydrogels, E-Polymers 17 (2017) 95–106, https://doi.org/10.1515/epoly-2016-0250.
[44] S. Sarkar, C. Hazra, M. Chatti, V. Sudarsan, V. Mahalingam, Enhanced quantum efficiency for Dy3+ emissions in water dispersible PbF2 nanocrystals, RSC Adv. 2 (2012) 8269, https://doi.org/10.1039/c2ra21113k.
[45] K. Zhang, Y. Zhuang, J. Li, X. Liu, S. He, Poly(acrylic acid)-modified MoS2 nanoparticle-based transdermal delivery of atenolol, Int. J. Nanomedicine 15 (2020) 5517–5526, https://doi.org/10.2147/IJN.S257906.
[46] A.S. Balaganesh R. Sengodan R. Ranjithkumar B. Chandarshekar , Synthesis and Characterization of Porous Calcium Oxide Nanoparticles (CaO NPS), Int. J. Innov. Technol. Explor. Eng. (n.d.) 2278–3075. doi:10.7324/RJC.2018.1111934.
[47] A.R. Butt, I.A. Butt, A. Nazir, M. Ikram, S. Sadiq, K. Rashid, T. Shujah, S. Ali, Molecular imaging of CaO nanowhiskers in living organs, Nucleus 52 (2015) 159–164, http://thenucleuspak.org.pk/index.php/Nucleus/article/view/633 (accessed May 20, 2022).
[48] S. Sinha, A. Kr, R.Kr. Aman, N. Singh, K.Shivani Kr, Calcium oxide(CaO) nanomaterial (Kukutanda twak Bhasma) from egg shell: green synthesis, physical properties and antimicrobial behaviour, Mater. Today Proc. 43 (2021) 3414–3419, https://doi.org/10.1016/j.matpr.2020.09.072.
[49] A. M.V., M. Harb, R. Sundaram, Synthesis and characterization of cellulose/TiO2 nanocomposite: evaluation of in vitro antibacterial and in silico molecular docking studies, Carbohydr. Polym. 249 (2020), 116868, https://doi.org/10.1016/j.carbpol.2020.116868.
[50] L. Lim, N. Rosli, I. Ahmad, A. Mat Lazim, M. Mohd Amin, Synthesis and swelling behavior of pH-sensitive semi-IPN superabsorbent hydrogels based on poly(acrylic acid)reinforced with cellulose nanocrystals, Nanomaterials 7 (2017) 399, https://doi.org/10.3390/nano7110399.
[51] A. Pinkert, K.N. Marsh, S. Pang, M.P. Staiger, Ionic liquids and their interaction with cellulose, Chem. Rev. 109 (2009) 6712–6728, https://doi.org/10.1021/CR9001947/ASSET/CR9001947.FP.PNG_V03.
[52] Y. Wu, L. Wang, Y. Qing, N. Yan, C. Tian, Y. Huang, A green route to prepare fluorescent and absorbent nano-hybrid hydrogel for water detection, Sci. Rep. 7 (2017) 4380, https://doi.org/10.1038/s41598-017-04542-7.
[53] A. Imtiaz, M.A. Farrukh, M. Khaleeq-ur-rahman, R. Adnan, Micelle-assisted synthesis of Al 2 O 3 ·CaO nanocatalyst: optical properties and their applications in photodegradation of 2,4,6-trinitrophenol, Sci. World J. 2013 (2013) 1–11, https://doi.org/10.1155/2013/641420.
[54] H.-Y. Yu, G.-Y. Chen, Y.-B. Wang, J.-M. Yao, A facile one-pot route for preparing cellulose nanocrystal/zinc oxide nanohybrids with high antibacterial and photocatalytic activity, Cellulose 22 (2015) 261–273, https://doi.org/10.1007/s10570-014-0491-0.
[55] M. Todica, C.V. Pop, R. Stefan, M. Nagy, S. Garabagiu, Spectroscopic investigation of some poly (acrylic acid) gels with embedded gold nanoparticles, Stud. Univ. Babes-Bolyai Chem. 60 (2015) 19–28, https://www.researchgate.net/profile/Pop-Cornel/publication/283127367_Spectroscopic_investigation_of_some_poly_acrylic_acid_gels_with_embedded_gold_nanoparticles/links/5913fb1caca27200fe4b595e/Spectroscopic-investigation-of-some-poly-acrylic-acid-gels-wit (accessed April 19, 2022).
[56] H. Kaczmarek, M. Metzler, The properties of poly (acrylic acid) modified with NPhenylbenzothioamide as potential drug carriers, Open Process Chem. J. 6 (2014) 1–7, https://doi.org/10.2174/1875180601406010001.
[57] (17) (PDF) CaO nanoparticles as a potential drug delivery agent for biomedical applications, Thesis Diss. Repos, https://www.researchgate.net/publication/281439087_CaO_nanoparticles_as_a_potential_drug_delivery_agent_for_biomedical_applications. https://ir.lib.uwo.ca/etd/879 (accessed April 26, 2022).
[58] (10) (PDF) A comparative study on Photocatalytic degradation of Violet GL2B azo dye using CaO and TiO 2 nanoparticles (n.d.), https://www.researchgate.net/publication/331988049_A_comparative_study_on_Photocatalytic_degradation_of_Violet_GL2B_azo_dye_using_CaO_and_TiO_2_nanoparticles (accessed May 20, 2022).
[59] A.M. Raba-Páez, J.O.D. Malafatti, C.A. Parra-Vargas, E.C. Paris, M. Rincón-Joya, Effect of tungsten doping on the structural, morphological and bactericidal properties of nanostructured CuO, PLoS One 15 (2020), e0239868, https://doi.org/10.1371/journal.pone.0239868.
[60] F. Henry, P. Marchal, J. Bouillard, A. Vignes, O. Dufaud, L. Perrin, The effect of agglomeration on the emission of particles from nanopowders flow, in: Chem. Eng. Trans, 2013, pp. 811–816, https://doi.org/10.3303/CET1331136.
[61] S. Bashir, Y.Y. Teo, S. Ramesh, K. Ramesh, Synthesis and characterization of karaya gum-g-poly (acrylic acid) hydrogels and in vitro release of hydrophobic quercetin, Polymer 147 (2018) 108–120, https://doi.org/10.1016/J.POLYMER.2018.05.071 (Guildf).
[62] M.M. Rahman, M.B. Islam, M. Biswas, A.H.M. Khurshid Alam, In vitro antioxidant and free radical scavenging activity of different parts of Tabebuia pallida growing in Bangladesh, BMC Res.Notes 8 (2015) 621, https://doi.org/10.1186/s13104-015-1618-6.
[63] A. Mobasheri, H.K. Biesalski, M. Shakibaei, Y. Henrotin, Antioxidants and osteoarthritis, in: Syst. Biol. Free Radicals Antioxidants, SpringerBerlin Heidelberg, Berlin, Heidelberg, 2014, pp. 2997–3026, https://doi.org/10.1007/978-3-642-30018-9_130.
[64] K. Kandiah, T. Jeevanantham, B. Ramasamy, in: Reliability of antioxidant potential and in vivo compatibility with extremophilic actinobacterial-mediated magnesium oxide nanoparticle synthesis 47, 2019, pp. 862–872, https://doi.org/10.1080/21691401.2019.1580287.
[65] T.S. Thring, P. Hili, D.P. Naughton, Antioxidant and potential anti-inflammatory activity of extracts and formulations of white tea, rose, and witch hazel on primary human dermal fibroblast cells, J. Inflamm. 8 (2011) 27, https://doi.org/10.1186/1476-9255-8-27.
[66] V.R. Winrow, P.G. Winyard, C.J. Morris, D.R. Blake, Free radicals in inflammation: second messengers and mediators of tissue destruction, Br. Med. Bull. 49 (1993) 506–522, https://doi.org/10.1093/oxfordjournals.bmb.a072627.
[67] A. Marino, I. Paterniti, M. Cordaro, R. Morabito, M. Campolo, M. Navarra, E. Esposito, S. Cuzzocrea, Role of natural antioxidants and potential use of

bergamot in treating rheumatoid arthritis, PharmaNutrition 3 (2015) 53–59, https://doi.org/10.1016/j.phanu.2015.03.002.
[68] A. Haider, M. Ijaz, S. Ali, J. Haider, M. Imran, H. Majeed, I. Shahzadi, M.M. Ali, J. A. Khan, M. Ikram, Green synthesized phytochemically (Zingiber officinale and Allium sativum) reduced nickel oxide nanoparticles confirmed bactericidal and catalytic potential, Nanoscale Res. Lett. 15 (2020) 50, https://doi.org/10.1186/s11671-020-3283-5.
[69] J. Chen, J. Liu, Y. Hu, Z. Tian, Y. Zhu, in: Metal-organic framework-coated magnetite nanoparticles for synergistic magnetic hyperthermia and chemotherapy with pH-triggered drug release 20, 2019, pp. 1043–1054, https://doi.org/10.1080/14686996.2019.1682467. Http://Www.Tandfonline.Com/Action/JournalInformation?Show=aimsScope&journalCode=tsta20#.VmBmuzZFCUk.
[70] Y. Zhang, C. Yang, W. Wang, J. Liu, Q. Liu, F. Huang, L. Chu, H. Gao, C. Li, D. Kong, Q. Liu, J. Liu, Co-delivery of doxorubicin and curcumin by pH-sensitive prodrug nanoparticle for combination therapy of cancer, Sci. Rep. 6 (2016) 21225, https://doi.org/10.1038/srep21225.